Available online at www.sciencedirect.com
SCIENCE DIRECT®
Journal of Computational Physics 201 (2004) 238–260
JOURNAL OF COMPUTATIONAL PHYSICS
www.elsevier.com/locate/jcp

Finite-volume WENO schemes for three-dimensional conservation laws

V.A. Titarev [a,*], E.F. Toro [b]

[a] Department of Mathematics, Faculty of Science, University of Trento, Trento, Italy
[b] Laboratory of Applied Mathematics, Faculty of Engineering, University of Trento, Trento, Italy

Received 25 August 2003; received in revised form 15 February 2004; accepted 20 May 2004
Available online 8 July 2004

Abstract

In this paper we firstly carry out an extension of the finite-volume WENO schemes to three space dimensions and higher orders of accuracy. Secondly, we propose to use more accurate fluxes as the building block. These are the HLLC and MUSTA fluxes [Multi-stage predictor–corrector fluxes for hyperbolic equations, 2003; Restoration of the contact surface in the HLL Riemann solver, Report CoA 9204, June 1992; J. Shock Waves 4 (1994) 25]. The numerical results suggest that the new WENO-HLLC and WENO-MUSTA schemes compare satisfactorily with the state-of-the-art finite-volume scheme of Shi et al. [J. Comput. Phys. 175 (2002) 108].

Keywords: High-order schemes; Weighted essentially non-oscillatory; HLLC flux; FORCE flux; MUSTA flux; Two and three space dimensions

1. Introduction

The motivation of this paper is to develop improved finite-volume weighted essentially non-oscillatory (WENO) schemes [6,9,12,14]. The improvements are twofold. Firstly, we generalize the existing two-dimensional schemes [6,14] to three space dimensions. We consider schemes with piece-wise parabolic (fifth order) and piece-wise cubic (seventh order) reconstructions and provide the precise information on the WENO reconstruction weights and values for the Gaussian integration points over cell faces so that the schemes can be easily coded. Secondly, we propose to use more accurate upwind HLLC and MUSTA fluxes as the building block in the WENO schemes. The HLLC flux [17,19,20] contains all waves in the Riemann problem solution, does not use linearizations of the equations and works well for low-density problems and sonic points without adhoc fixes. The recent upwind Multi-Stage (MUSTA) flux [18] achieves upwinding by

* Corresponding author.
E-mail addresses: titarev@science.unitn.it (V.A. Titarev), toro@ing.unitn.it (E.F. Toro).
URLs: http://www.science.unitn.it/~titarev, http://www.ing.unitn.it/toro.

0021-9991/$ - see front matter
doi:10.1016/j.jcp.2004.05.015

evolving in time the initial data for the local Riemann problem via governing equations and thus does not need any information on the details of the Riemann problem solution. Some researches would refer to this scheme as the *Riemann-solver-free* upwind scheme.

We present numerical results of our new WENO-HLLC and WENO-MUSTA schemes in one, two and three space dimensions. In particular, the convergence studies for the vortex evolution problem [14] and the double Mach reflection problem [23] demonstrate that our schemes compare satisfactorily with the state-of-the art finite-volume WENO scheme of Shi et al. [14].

The rest of the paper is organised as follows. In Section 2 we describe the general semi-discrete WENO framework in three space dimensions. In Section 3 we give all details on the reconstruction procedure in three space dimensions. The HLLC and MUSTA fluxes are reviewed in Section 4. Numerical results of the new WENO-HLLC and WENO-MUSTA schemes in one, two and three space dimensions are presented in Section 5. Conclusions are drawn in Section 6.

2. General framework in three space dimensions

Consider three-dimensional hyperbolic systems in conservation form

$$\partial_t \mathbf{Q} + \partial_x \mathbf{F}(\mathbf{Q}) + \partial_y \mathbf{G}(\mathbf{Q}) + \partial_z \mathbf{H}(\mathbf{Q}) = \mathbf{0}, \tag{1}$$

where $\mathbf{Q}(x, y, z, t)$ is the vector of unknown conservative variables and $\mathbf{F}(\mathbf{Q})$, $\mathbf{G}(\mathbf{Q})$ and $\mathbf{H}(\mathbf{Q})$ are physical flux vectors in x, y and z coordinate directions, respectively. Let I_{ijk} be a control volume (a computational cell) in x–y–z space

$$I_{ijk} = \left[x_{i-1/2}, x_{i+1/2}\right] \times \left[y_{j-1/2}, y_{j+1/2}\right] \times \left[z_{k-1/2}, z_{k+1/2}\right],$$

with the dimensions given by $\Delta x = x_{i+1/2} - x_{i-1/2}$, $\Delta y = y_{j+1/2} - y_{j-1/2}$, $\Delta z = z_{k+1/2} - z_{k-1/2}$.

Integrating (1) over I_{ijk}, we obtain the following semi-discrete relations:

$$\frac{\mathrm{d}}{\mathrm{d}t}\mathbf{Q}_{ijk}(t) = \frac{1}{\Delta x}\left(\mathbf{F}_{i-1/2,jk} - \mathbf{F}_{i+1/2,jk}\right) + \frac{1}{\Delta y}\left(\mathbf{G}_{i,j-1/2,k} - \mathbf{G}_{i,j+1/2,k}\right) + \frac{1}{\Delta z}\left(\mathbf{H}_{ij,k-1/2} - \mathbf{H}_{ij,k+1/2}\right), \tag{2}$$

where $\mathbf{Q}_{ijk}(t)$ is the spatial average of the solution in cell I_{ijk} at time t

$$\mathbf{Q}_{ijk}(t) = \frac{1}{\Delta x}\frac{1}{\Delta y}\frac{1}{\Delta z}\int_{x_{i-1/2}}^{x_{i+1/2}}\int_{y_{j-1/2}}^{y_{j+1/2}}\int_{z_{k-1/2}}^{z_{k+1/2}} \mathbf{Q}(x, y, z, t)\,\mathrm{d}z\,\mathrm{d}y\,\mathrm{d}x \tag{3}$$

and $\mathbf{F}_{i+1/2,jk}$, $\mathbf{G}_{i,j+1/2,k}$ and $\mathbf{H}_{ij,k+1/2}$ are spatial averages of physical fluxes over cell faces at time t:

$$\begin{aligned}
\mathbf{F}_{i+1/2,jk} &= \frac{1}{\Delta y}\frac{1}{\Delta z}\int_{y_{j-1/2}}^{y_{j+1/2}}\int_{z_{k-1/2}}^{z_{k+1/2}} \mathbf{F}(\mathbf{Q}(x_{i+1/2}, y, z, t))\,\mathrm{d}z\,\mathrm{d}y,\\
\mathbf{G}_{i,j+1/2,k} &= \frac{1}{\Delta x}\frac{1}{\Delta z}\int_{x_{i-1/2}}^{x_{i+1/2}}\int_{z_{k-1/2}}^{z_{k+1/2}} \mathbf{G}(\mathbf{Q}(x, y_{j+1/2}, z, t))\,\mathrm{d}z\,\mathrm{d}x,\\
\mathbf{H}_{ij,k+1/2} &= \frac{1}{\Delta x}\frac{1}{\Delta y}\int_{x_{i-1/2}}^{x_{i+1/2}}\int_{y_{j-1/2}}^{y_{j+1/2}} \mathbf{H}(\mathbf{Q}(x, y, z_{k+1/2}, t))\,\mathrm{d}y\,\mathrm{d}x.
\end{aligned} \tag{4}$$

Expressions (3) and (4) so far are exact relations, but can also be used in the construction of high-order accurate semi-discrete schemes if $\mathbf{Q}_{ijk}(t)$, $\mathbf{F}_{i+1/2,jk}$, $\mathbf{G}_{i,j+1/2,k}$ and $\mathbf{H}_{ij,k+1/2}$ are regarded as numerical approximations to the corresponding exact quantities. Let us denote these approximations by the same symbols as the exact values in (3) and (4). The simplest scheme which can be considered from the above

framework results from assuming initial data at time t^n as given by a set of piece-wise constant values $\mathbf{Q}_{ijk}$ and using the Euler time-stepping to discretize the time derivative. Godunov [5] first proposed to use the Riemann problem solution for the computation of numerical fluxes resulting in his famous first-order conservative upwind scheme. A popular approach to the construction of second order Godunov methods, pioneered by Kolgan [10,11] and developed further by van Leer [21], relies on piece-wise linear reconstruction of data inside each computational cell. Finally, finite-volume essentially non-oscillatory schemes [2,8,14] can be regarded as uniformly high order extensions of this approach in two space dimensions in which the data is represented by polynomials of arbitrary order and TVD Runge–Kutta methods are used for the discretization of the ODE system (2).

The procedure to evaluate numerical fluxes (4) in three space dimensions is a straightforward extension of the corresponding two-dimensional one and consists of three main steps. The first step is to discretize the integrals over the faces (4) using a suitable Gaussian numerical quadrature. For the rest of the paper we shall concentrate on $\mathbf{F}_{i+1/2,jk}$; the expressions for $\mathbf{G}_{i,j+1/2,k}$ and $\mathbf{H}_{ij,k+1/2}$ are obtained in an entirely analogous manner. The application of the tensor product of a one-dimensional N-point quadrature rule to (4) yields the following expression for the flux in the x coordinate direction:

$$\mathbf{F}_{i+1/2,j,k} = \frac{1}{\Delta y}\frac{1}{\Delta z}\sum_{\alpha=1}^{N}\sum_{\beta=1}^{N}\mathbf{F}(\mathbf{Q}(x_{i+1/2}, y_\alpha, z_\beta))K_\beta K_\alpha, \tag{5}$$

where the subscripts $\alpha, \beta = 1, \ldots, N$ correspond to different Gaussian integration points y_α, z_β and weights K_α, K_β. Expression (5) involves point-wise values of $\mathbf{Q}$ whereas the scheme evolves the cell averages of $\mathbf{Q}$. Thus the second step in evaluating the fluxes is to reconstruct the point-wise values of the solution from cell averages and obtain high-order accurate approximations to the values of $\mathbf{Q}$ at the integration points. In WENO schemes this is achieved by means of a weighted essentially non-oscillatory (WENO) adaptive-stencil reconstruction procedure [7,12], which estimates the smoothness of the solution and builds the reconstruction polynomial in such a way so as to avoid interpolation across discontinuities. After the reconstruction is carried out at each face we have two sets of values of $\mathbf{Q}$, corresponding to $x_{i+1/2} - 0$ and $x_{i+1/2} + 0$ which are often called left and right boundary extrapolated values:

$$\mathbf{Q}^{\mathrm{L}}_{i+1/2,\alpha\beta} = \mathbf{Q}(x_{i+1/2} - 0, y_\alpha, z_\beta), \quad \mathbf{Q}^{\mathrm{R}}_{i+1/2,\alpha\beta} = \mathbf{Q}(x_{i+1/2} + 0, y_\alpha, z_\beta). \tag{6}$$

The last step in the evaluation of the fluxes is to replace $\mathbf{F}(\mathbf{Q}(x_{i+1/2}, y_\alpha, z_\beta))$ in (5) by a certain monotone function of left and right boundary extrapolated values $\hat{\mathbf{F}}(\mathbf{Q}^{\mathrm{L}}, \mathbf{Q}^{\mathrm{R}})$, the building block of the WENO scheme, or numerical flux

$$\mathbf{F}_{i+1/2,j,k} = \frac{1}{\Delta y}\frac{1}{\Delta z}\sum_{\alpha=1}^{N}\sum_{\beta=1}^{N}\hat{\mathbf{F}}(\mathbf{Q}^{\mathrm{L}}_{i+1/2,\alpha\beta}, \mathbf{Q}^{\mathrm{R}}_{i+1/2,\alpha\beta})K_\beta K_\alpha. \tag{7}$$

To retain uniformly high order of time accuracy the solution is advanced in time by means of TVD Runge–Kutta methods. In this paper we use the following third order method of Shu [15]:

$$\begin{aligned}
\mathbf{Q}^{(1)}_{ijk} &= \mathbf{Q}^{n}_{ijk} + \Delta t\mathbf{L}_{ijk}(\mathbf{Q}^{n}),\\
\mathbf{Q}^{(2)}_{ijk} &= \frac{3}{4}\mathbf{Q}^{n}_{ijk} + \frac{1}{4}\mathbf{Q}^{(1)}_{ijk} + \frac{1}{4}\Delta t\mathbf{L}_{ijk}(\mathbf{Q}^{(1)}),\\
\mathbf{Q}^{n+1}_{ijk} &= \frac{1}{3}\mathbf{Q}^{n}_{ijk} + \frac{2}{3}\mathbf{Q}^{(2)}_{ijk} + \frac{2}{3}\Delta t\mathbf{L}_{ijk}(\mathbf{Q}^{(2)}),
\end{aligned} \tag{8}$$

where $\mathbf{L}_{ijk}(\mathbf{Q})$ denotes the spatial operator (right-hand side of (2)) at the appropriate time level. The above procedure of flux evaluation must be carried out during each stage of the Runge–Kutta method.

The explicit scheme considered above requires the computation of a time step Δt to be used in (8), such that stability of the numerical method is ensured. One way of choosing Δt is

$$\Delta t = C_{\mathrm{cfl}} \times \min_{ijk} \left(\frac{\Delta x}{|S_{ijk}^{n,x}|}, \frac{\Delta y}{|S_{ijk}^{n,y}|}, \frac{\Delta z}{|S_{ijk}^{n,z}|} \right). \tag{9}$$

Here $S_{ijk}^{n,d}$ is the speed of the fastest wave present at time level n travelling in the d direction, with $d = x, y, z$. C_{cfl} is the CFL number and is chosen according to the linear stability condition of the scheme. When the three-stage Runge–Kutta method (8) is used in one space dimension the WENO schemes have the optimal stability condition of Courant number

$$0 < C_{\mathrm{cfl}} \leqslant 1. \tag{10}$$

The two-dimensional and three-dimensional schemes have the reduced stability conditions, which in fact coincide with those of the unsplit Godunov scheme in two and three space dimensions. In two space dimensions the stability condition is

$$0 < C_{\mathrm{cfl}} \leqslant 1/2. \tag{11}$$

Our numerical experiments show that in three space dimensions the stability condition is

$$0 < C_{\mathrm{cfl}} \leqslant 1/3. \tag{12}$$

The description of the scheme is complete when an algorithm to calculate the values of $\mathbf{Q}$ at Gaussian integration points is given and a flux function $\hat{\mathbf{F}}(\mathbf{Q}^{\mathrm{L}}, \mathbf{Q}^{\mathrm{R}})$ is chosen. In the following sections we give details on the WENO reconstruction and the numerical flux. It is sufficient to explain the general three-dimensional case; the two- and one-dimensional cases will follow easily.

3. WENO reconstruction in three space dimensions

3.1. Scalar finite-volume reconstruction

The reconstruction problem we face is the following. Given spatial averages of a scalar function $q(x, y, z)$ in a cell I_{ijk}

$$q_{ijk} = \frac{1}{\Delta x}\frac{1}{\Delta y}\frac{1}{\Delta z}\int_{x_{i-1/2}}^{x_{i+1/2}}\int_{y_{j-1/2}}^{y_{j+1/2}}\int_{z_{k-1/2}}^{z_{k+1/2}} q(x, y, z)\,\mathrm{d}z\,\mathrm{d}y\,\mathrm{d}x, \tag{13}$$

we want to compute the point-wise value of q at Gaussian integration points $(x_{i+1/2}, y_\alpha, z_\beta)$ so that the reconstruction procedure is conservative and these reconstructed values are of high-order of accuracy. There are essentially two ways of accomplishing this: genuine multidimensional reconstruction and dimension-by-dimension reconstruction. The genuine multidimensional reconstruction [14] considers all cells in the multidimensional stencil simultaneously to build up a reconstruction polynomial, whereas dimension-by-dimension reconstruction [2,14] consists of a number of one-dimensional reconstruction sweeps. The dimension-by-dimension reconstruction is much simpler and less computationally expensive than the genuine multidimensional one; this is especially so in three space dimensions. Therefore, in this paper we use dimension-by-dimension reconstruction throughout.

The general idea of dimension-by-dimension reconstruction in two space dimensions is explained in [2] in the context of the ENO schemes. The extension to three space dimensions is straightforward and consists of

three steps. Recall that we need left $q^{\mathrm{L}}_{i+1/2,\alpha\beta}$ and right $q^{\mathrm{R}}_{i+1/2,\alpha\beta}$ extrapolated values. For the left values the stencil consists of cells $I_{i_x i_y i_z}$ such that

$$i - r \leqslant i_x \leqslant i + r, \quad j - r \leqslant i_y \leqslant j + r, \quad k - r \leqslant i_z \leqslant k + r, \tag{14}$$

where $r - 1$ is the order of polynomials used in WENO sweeps, e.g. $r = 3$ corresponds to the weighted piece-wise parabolic (fifth order) reconstruction and so on. For the right values the stencil consists of cells for which $i + 1 - r \leqslant i_x \leqslant i + 1 + r$ and i_y, i_z vary according to (14).

In the first step of the three-dimensional reconstruction for all indexes i_y, i_z from the stencil we perform the one-dimensional WENO reconstruction in the x coordinate direction (normal to the cell face) and obtain two-dimensional averages with respect to y–z coordinate directions:

$$\begin{aligned} v^{\mathrm{L}}_{i_y i_z} &= \frac{1}{\Delta y}\frac{1}{\Delta z}\int_{y_{i_y-1/2}}^{y_{i_y+1/2}}\int_{z_{i_z-1/2}}^{z_{i_z+1/2}} q(x_{i+1/2} - 0, y, z)\,\mathrm{d}z\,\mathrm{d}y, \\ v^{\mathrm{R}}_{i_y i_z} &= \frac{1}{\Delta y}\frac{1}{\Delta z}\int_{y_{i_y-1/2}}^{y_{i_y+1/2}}\int_{z_{i_z-1/2}}^{z_{i_z+1/2}} q(x_{i+1/2} + 0, y, z)\,\mathrm{d}z\,\mathrm{d}y. \end{aligned} \tag{15}$$

In the second step we perform one-dimensional reconstruction in y coordinate direction for all values of i_z and obtain one-dimensional averages of the solution with respect to z coordinate direction

$$\begin{aligned} w^{\mathrm{L}}_{i_z} &= \frac{1}{\Delta z}\int_{z_{i_z-1/2}}^{z_{i_z+1/2}} q(x_{i+1/2} - 0, y_\alpha, z)\,\mathrm{d}z, \\ w^{\mathrm{R}}_{i_z} &= \frac{1}{\Delta z}\int_{z_{i_z-1/2}}^{z_{i_z+1/2}} q(x_{i+1/2} + 0, y_\alpha, z)\,\mathrm{d}z \end{aligned} \tag{16}$$

in lines corresponding to the Gaussian integration points on the y axis ($x = x_{i+1/2}$, $y = y_\alpha$). Finally, for each line ($x = x_{i+1/2}$, $y = y_\alpha$) we obtain reconstructed point-wise values $q(x_{i+1/2}, y_\alpha, z_\beta)$ by again applying the one-dimensional reconstruction now to $w^{\mathrm{L}}_{i_z}$, $w^{\mathrm{R}}_{i_z}$ in the z coordinate direction. We note that it is also possible to do the z sweep in the second step instead of y sweep.

The two-dimensional reconstruction is obtained by using only two first steps in the above algorithm.

We now proceed to define the reconstructed values for each of the one-dimensional WENO sweeps. We do so in terms of reconstructions of one-dimensional averages u_i of a function $u(\xi)$

$$u_i = \frac{1}{\Delta\xi}\int_{\xi_{i-1/2}}^{\xi_{i+1/2}} u(\xi)\,\mathrm{d}\xi, \tag{17}$$

where $\Delta\xi$ is the cell size: $\Delta\xi = \xi_{i+1/2} - \xi_{i-1/2}$. Recall that in one space dimension for any order of accuracy r there are r candidate stencils for reconstruction. For each such stencil of r cells there is a corresponding $(r-1)$th-order polynomial $p_l(\xi)$, $l = 0, \ldots, r-1$. The WENO reconstruction procedure [12,7] defines the reconstructed value as a convex combination of rth-order accurate values of all polynomials, taken with positive nonlinear weights. The weights are chosen in such a way as to achieve $(2r-1)$th order of accuracy when the solution is smooth and to mimic the ENO idea [8,2] otherwise. For a given point $\tilde{\xi}$ the design of weights consists of three steps. First, one finds the so-called optimal weights d_l so that the combination of all polynomials with these weights produces the value of the polynomial of order $(2r-1)$ corresponding to the large stencil. Next, if optimal weights d_l are all positive one defines the nonlinear weights ω_l as

$$\alpha_l = \frac{d_l}{(\varepsilon + \beta_l)^2}, \quad \omega_l = \frac{\alpha_k}{\sum_{l=0}^{r-1}\alpha_l}, \quad l = 0, \ldots r-1. \tag{18}$$

Here β_l are the so-called smoothness indicators [7]

$$\beta_l = \sum_{m=1}^{r-1} \int_{\xi_{i-1/2}}^{\xi_{i+1/2}} \left(\frac{\mathrm{d}^m}{\mathrm{d}x^m} p_l(\xi) \right)^2 \Delta\xi^{2m-1} \, \mathrm{d}\xi, \quad l = 0, \ldots, r-1. \tag{19}$$

If some of d_l are negative then a special procedure to handle such negative weights must be used, see [14] for details. The small constant ε is introduced to avoid division by zero when $\beta_l \equiv 0$; we usually set $\varepsilon = 10^{-6}$. The final WENO reconstructed value is then given by

$$u(\tilde{\xi}) = \sum_{l=0}^{r-1} p_l(\tilde{\xi}) w_l. \tag{20}$$

In several space dimensions the one-dimensional WENO procedure is applied during each one-dimensional sweep. For the first sweep (normal to the cell face) the weights are designed to obtain reconstructed values at $x_{i+1/2}$; the corresponding linear weights d_l and smoothness indicators β_l can be found in [1,7] for up to $r = 6$. For the second and third steps the weights, which will be different from the first step, are designed to achieve $(2r-1)$th order of accuracy for Gaussian integration points (y_α, z_β). The values of the weights are tailored to a specific Gaussian integration rule used to discretize the spatial integrals (5) and (7). Our numerical experiments show that the best results in terms of accuracy and computational cost for $r = 3, 4$ are obtained if the following two-point (fourth order) Gaussian quadrature is used:

$$\int_{-1}^{1} \varphi(\xi) \, \mathrm{d}\xi = \varphi\left(-\frac{1}{\sqrt{3}} \right) + \varphi\left(+\frac{1}{\sqrt{3}} \right), \tag{21}$$

even though the use of (21) leads to formal fourth order spatial accuracy. The WENO sweep in the x coordinate direction (normal to the cell face) corresponds to the left and right reconstructed values at $\xi_{i+1/2}$ whereas the y and z sweeps need values at the Gaussian points ξ_α; for the two-point quadrature (21) these are $\xi_i \pm \Delta\xi/(2\sqrt{3})$.

It appears as if the weights and reconstruction formulas for the Gaussian integration points ξ_α have not been reported in the literature so far. Therefore, in order to provide the complete information about the scheme below we give all necessary information for one dimensional sweeps in the piece-wise parabolic ($r = 3$) and piece-wise cubic ($r = 4$) reconstruction.

3.2. Piece-wise parabolic WENO reconstruction ($r = 3$)

We consider a cell $[\xi_{i-1/2}, \xi_{i+1/2}]$ and provide expressions for $u(\xi_{i+1/2} - 0)$, $u(\xi_{i-1/2} + 0)$ and $u(\xi_i \pm \Delta\xi/(2\sqrt{3}))$. The three candidate stencils for reconstruction are

$$S_0 = (i, i+1, i+2), \quad S_1 = (i-1, i, i+1), \quad S_2 = (i-2, i-1, i). \tag{22}$$

The corresponding smoothness indicators are given by [7]

$$\begin{aligned}
\beta_0 &= \frac{13}{12}(u_i - 2u_{i+1} + u_{i+2})^2 + \frac{1}{4}(3u_i - 4u_{i+1} + u_{i+2})^2, \\
\beta_1 &= \frac{13}{12}(u_{i-1} - 2u_i + u_{i+1})^2 + \frac{1}{4}(u_{i-1} - u_{i+1})^2, \\
\beta_2 &= \frac{13}{12}(u_{i-2} - 2u_{i-1} + u_i)^2 + \frac{1}{4}(u_{i-2} - 4u_{i-1} + 3u_i)^2.
\end{aligned} \tag{23}$$

The optimal weights d_l for the left extrapolated value $u^{\mathrm{L}}_{i+1/2}$ at $x_{i+1/2}$ are given by [7]

$$d_0 = \frac{3}{10}, \quad d_1 = \frac{3}{5}, \quad d_2 = \frac{1}{10} \tag{24}$$

and $u^{\mathrm{L}}_{i+1/2}$ is given by

$$\begin{aligned} u^{\mathrm{L}}_{i+1/2} &= u(\xi_{i+1/2} - 0) \\ &= \frac{1}{6}\omega_0(-u_{i+2} + 5u_{i+1} + 2u_i) + \frac{1}{6}\omega_1(-u_{i-1} + 5u_i + 2u_{i+1}) + \frac{1}{6}\omega_2(2u_{i-2} - 7u_{i-1} + 11u_i). \end{aligned} \tag{25}$$

The optimal weights d_l for right boundary extrapolated value $u^{\mathrm{R}}_{i-1/2}$ at $x_{i-1/2}$ are obtained by symmetry

$$d_0 = \frac{1}{10}, \quad d_1 = \frac{3}{5}, \quad d_2 = \frac{3}{10} \tag{26}$$

and $u^{\mathrm{R}}_{i-1/2}$ is given by

$$\begin{aligned} u^{\mathrm{R}}_{i-1/2} &= u(\xi_{i-1/2} + 0) \\ &= \frac{1}{6}\omega_0(2u_{i+2} - 7u_{i+1} + 11u_i) + \frac{1}{6}\omega_1(-u_{i+1} + 5u_i + 2u_{i-1}) + \frac{1}{6}\omega_2(-u_{i-2} + 5u_{i-1} + 2u_i). \end{aligned} \tag{27}$$

For the first Gaussian integration point $\xi = \xi_i - \Delta\xi/(2\sqrt{3})$ the optimal weights are as follows:

$$d_0 = \frac{210 - \sqrt{3}}{1080}, \quad d_1 = \frac{11}{18}, \quad d_2 = \frac{210 + \sqrt{3}}{1080} \tag{28}$$

and the reconstructed value is given by

$$\begin{aligned} u\left(\xi_i - \frac{\Delta\xi}{2\sqrt{3}}\right) = {} & \omega_0\left[u_i + (3u_i - 4u_{i+1} + u_{i+2})\frac{\sqrt{3}}{12}\right] + \omega_1\left[u_i - (-u_{i-1} + u_{i+1})\frac{\sqrt{3}}{12}\right] \\ & + \omega_2\left[u_i - (3u_i - 4u_{i-1} + u_{i-2})\frac{\sqrt{3}}{12}\right]. \end{aligned} \tag{29}$$

For the second Gaussian integration point $\xi = \xi_i + \Delta\xi/(2\sqrt{3})$ the optimal weights are obtained from symmetry by interchanging d_0 and d_2 in (28), namely

$$d_0 = \frac{210 + \sqrt{3}}{1080}, \quad d_1 = \frac{11}{18}, \quad d_2 = \frac{210 - \sqrt{3}}{1080}. \tag{30}$$

The reconstructed value is

$$\begin{aligned} u\left(\xi_i + \frac{\Delta\xi}{2\sqrt{3}}\right) = {} & \omega_0\left[u_i - (3u_i - 4u_{i+1} + u_{i+2})\frac{\sqrt{3}}{12}\right] + \omega_1\left[u_i - (u_{i-1} - u_{i+1})\frac{\sqrt{3}}{12}\right] \\ & + \omega_2\left[u_i - (-3u_i + 4u_{i-1} - v_{i-2})\frac{\sqrt{3}}{12}\right]. \end{aligned} \tag{31}$$

We note that the nonlinear weights ω_l must be computed according to (18) *separately* for each of the points $\xi_i \pm \Delta\xi/(2\sqrt{3})$.

3.3. Piece-wise cubic WENO reconstruction ($r = 4$)

The four candidate stencils are

$$\begin{aligned} S_0 &= (i, i+1, i+2, i+3), \quad S_1 = (i-1, i, i+1, i+2), \\ S_2 &= (i-2, i-1, i, i+1), \quad S_3 = (i-3, i-2, i-1, i). \end{aligned} \tag{32}$$

The corresponding smoothness indicators as well as expressions for $u^{\mathrm{L}}_{i+1/2}$ and $u^{\mathrm{R}}_{i-1/2}$ are rather cumbersome and can be found in [1]. We omit them to save space and describe the weights and reconstructed values only for the Gaussian integration points.

For the first Gaussian integration point $\xi = \xi_i - \Delta\xi/(2\sqrt{3})$ the optimal weights are as follows:

$$\begin{aligned} d_0 &= \frac{-50\sqrt{3}+3717}{166320}, \\ d_1 &= \frac{72\sqrt{3}}{7}\left(\frac{889\sqrt{3}}{63360} - \frac{587}{1995840}\right), \\ d_2 &= \frac{72\sqrt{3}}{7}\left(\frac{889\sqrt{3}}{63360} + \frac{587}{1995840}\right), \\ d_3 &= \frac{50\sqrt{3}+3717}{166320} \end{aligned} \tag{33}$$

and the reconstructed value is given by

$$\begin{aligned} & u\left(\xi_i - \frac{\Delta\xi}{2\sqrt{3}}\right) \\ &= \omega_0\left[u_i - (-43u_i + 69u_{i+1} - 33u_{i+2} + 7u_{i+3})\frac{\sqrt{3}}{144} - (-u_i + 3u_{i+1} - 3u_{i+2} + u_{i+3})\frac{\sqrt{3}}{432}\right] \\ &\quad + \omega_1\left[u_i - (-15u_i + 27u_{i+1} - 7u_{i-1} - 5u_{i+2})\frac{\sqrt{3}}{144} + (-3u_i + 3u_{i+1} + u_{i-1} - u_{i+2})\frac{\sqrt{3}}{432}\right] \\ &\quad + \omega_2\left[u_i - (15u_i + 7u_{i+1} - 27u_{i-1} + 5u_{i-2})\frac{\sqrt{3}}{144} + (3u_i - u_{i+1} - 3u_{i-1} + u_{i-2})\frac{\sqrt{3}}{432}\right] \\ &\quad + \omega_3\left[u_i - (43u_i - 69u_{i-1} + 33u_{i-2} - 7u_{i-3})\frac{\sqrt{3}}{144} - (u_i - 3u_{i-1} + 3u_{i-2} - u_{i-3})\frac{\sqrt{3}}{432}\right]. \end{aligned} \tag{34}$$

For the second Gaussian integration point $\xi = \xi_i + \Delta\xi/(2\sqrt{3})$ optimal weights are obtained from symmetry by interchanging d_0 and d_2:

$$
\begin{aligned}
d_0 &= \frac{50\sqrt{3}+3717}{166320},\\
d_1 &= \frac{72\sqrt{3}}{7}\left(\frac{889\sqrt{3}}{63360}+\frac{587}{1995840}\right),\\
d_2 &= \frac{72\sqrt{3}}{7}\left(\frac{889\sqrt{3}}{63360}-\frac{587}{1995840}\right),\\
d_3 &= \frac{-50\sqrt{3}+3717}{166320}.
\end{aligned}
\tag{35}
$$

The reconstructed value is

$$
\begin{aligned}
&u\left(\xi_i+\frac{\Delta\xi}{2\sqrt{3}}\right)\\
&\quad=\omega_0\left[u_i+(-43u_i+69u_{i+1}-33u_{i+2}+7u_{i+3})\frac{\sqrt{3}}{144}+(-u_i+3u_{i+1}-3u_{i+2}+u_{i+3})\frac{\sqrt{3}}{432}\right]\\
&\qquad+\omega_1\left[u_i+(-15u_i+27u_{i+1}-7u_{i-1}-5u_{i+2})\frac{\sqrt{3}}{144}-(-3u_i+3u_{i+1}+u_{i-1}-u_{i+2})\frac{\sqrt{3}}{432}\right]\\
&\qquad+\omega_2\left[u_i+(15u_i+7u_{i+1}-27u_{i-1}+5u_{i-2})\frac{\sqrt{3}}{144}-(3u_i-u_{i+1}-3u_{i-1}+u_{i-2})\frac{\sqrt{3}}{432}\right]\\
&\qquad+\omega_3\left[u_i+(43u_i-69u_{i-1}+33u_{i-2}-7u_{i-3})\frac{\sqrt{3}}{144}+(u_i-3u_{i-1}+3u_{i-2}-u_{i-3})\frac{\sqrt{3}}{432}\right].
\end{aligned}
\tag{36}
$$

3.4. Reconstruction for systems

The reconstruction for systems can be carried out either in conservative variables or in local characteristic variables, see e.g. [8]. For the first option the above expressions (24)–(36) are used for each component of the vector of conservative variables $\mathbf{Q}$. For the characteristic reconstruction one first transforms to characteristic variables and then applies (24)–(36) to each component of these variables. The final values are obtained by transforming back to conservative variables.

Although the use of characteristic decomposition in reconstruction increases the computational cost of the scheme, our experiments show that in some cases it is necessary in order to avoid spurious oscillations. Therefore, in this paper we always carry out reconstruction in local characteristic variables.

A note needs to be added on the use of the ENO and WENO reconstructions for nonlinear systems. In general, ENO reconstruction avoids generating large O(1) oscillations near discontinuities by selecting a smooth stencil of $r-1$ cells out of r possible stencils covering the given cell. WENO reconstruction mimics the behavior of the ENO reconstruction near discontinuities by assigning nearly zero weights to stencils which cross a discontinuity. However, if the solution contains two discontinuities which are too close to each other the reconstruction procedure will not be able to find a smooth stencil and spurious oscillations will appear. As a result, the scheme may crash.

To avoid the above problem we adopt (with appropriate modifications for the present study) a method proposed in [8]. Consider computation of the left boundary extrapolated values for the cell I_{ijk} used in the

evaluation of the numerical flux $\mathbf{F}_{i+1/2,jk}$. For each Gaussian integration point $(x_{i+1/2}-0, y_\alpha, z_\beta)$ we check the following conditions:

$$|\rho(x_{i+1/2}-0, y_\alpha, z_\beta) - \rho_{ijk}| \leqslant 0.9\rho_{ijk}, \quad |p(x_{i+1/2}-0, y_\alpha, z_\beta) - p_{ijk}| \leqslant 0.9p_{ijk}. \tag{37}$$

If conditions (37) are not satisfied we decrease the order of reconstruction r in each of the one-dimensional WENO sweeps and repeat the reconstruction step for the left boundary extrapolated values. If conditions (37) are not satisfied even for the weighted piece-wise linear ($r = 2$) reconstruction we switch to a MUSCL-type reconstruction in each of the one-dimensional sweeps:

$$u^{\mathrm{L}}_{i+1/2} = u_i + \frac{\Delta\xi}{2}S, \quad u^{\mathrm{R}}_{i-1/2} = u_i - \frac{\Delta\xi}{2}S, \quad u\left(\xi_i \pm \frac{\Delta\xi}{2\sqrt{3}}\right) = u_i \pm \frac{\Delta\xi}{2\sqrt{3}}S, \tag{38}$$

where S is the limited slope. We use minmod-type limiter [10]

$$S = \frac{1}{2}(\mathrm{sign}(\Delta_-) + \mathrm{sign}(\Delta_+))\min(|\Delta_-|, |\Delta_+|), \quad \Delta_- = \frac{u_i - u_{i-1}}{\Delta\xi}, \quad \Delta_+ = \frac{u_{i+1} - u_i}{\Delta\xi}.$$

The right boundary extrapolated values are treated in an entirely analogous manner.

Our numerical experiments show that the use of a less diffusive slope limiter does not improve the accuracy and may sacrifice the robustness of the scheme.

We remark that the use of the above procedure does not in any way degrade the high order of accuracy of the schemes for smooth solutions; see [8] for details.

4. Numerical flux

In this section for simplicity we omit subscripts α, β of Gaussian integration points and write $\mathbf{Q}_{\mathrm{L}} \equiv \mathbf{Q}^{\mathrm{L}}_{i+1/2,\alpha\beta}$, $\mathbf{Q}_{\mathrm{R}} \equiv \mathbf{Q}^{\mathrm{R}}_{i+1/2,\alpha\beta}$. We also omit the hat over the numerical flux used as the building block.

Godunov [5] first introduced the idea of using the self-similar solution $\mathbf{Q}_*(s/\tau)$, $s = x - x_{i+1/2}$, $\tau = t - t^n$, of the following local Riemann problem to compute the upwind numerical flux

$$\partial_t\mathbf{Q} + \partial_x\mathbf{F} = \mathbf{0}, \quad \mathbf{Q}(x,0) = \begin{cases} \mathbf{Q}_{\mathrm{L}}, & x < x_{i+1/2}, \\ \mathbf{Q}_{\mathrm{R}}, & x > x_{i+1/2}. \end{cases} \tag{39}$$

The original Godunov scheme uses the exact Riemann solver and the flux is given as $\mathbf{F}_{i+1/2} = \mathbf{F}(\mathbf{Q}_*(0))$. More generally, the numerical flux can be defined as a monotone function of left and right extrapolated values $\mathbf{Q}_L$, $\mathbf{Q}_R$

$$\mathbf{F}_{i+1/2} = \mathbf{F}_{i+1/2}(\mathbf{Q}_{\mathrm{L}}, \mathbf{Q}_{\mathrm{R}}).$$

Below we briefly review the new upwind fluxes to be used in the framework of our schemes.

4.1. The HLLC flux

We specialize the presentation of the HLLC flux [19,20] as applied to the three-dimensional compressible Euler equations for a gamma-law gas of the form (1) with

$$\mathbf{Q}=\begin{pmatrix}\rho\\ \rho u\\ \rho v\\ \rho w\\ E\end{pmatrix},\quad \mathbf{F}=\mathbf{Q}u+\begin{pmatrix}0\\ p\\ 0\\ 0\\ pu\end{pmatrix},\quad \mathbf{G}=\mathbf{Q}v+\begin{pmatrix}0\\ 0\\ p\\ 0\\ pv\end{pmatrix},\quad \mathbf{H}=\mathbf{Q}w+\begin{pmatrix}0\\ 0\\ 0\\ p\\ pw\end{pmatrix},$$
$$p=(\gamma-1)(E-\frac{1}{2}\rho(u^2+v^2+w^2)), \tag{40}$$

where ρ, u, v, w p and E are density, components of velocity in the x, y and z coordinate directions, pressure and total energy, respectively; γ is the ratio of specific heats. An updated version of HLLC for the split 3D Euler equations is found in [17]. Assuming a three-wave structure with wave speed estimates S_{L}, S_* and S_{R} the HLLC flux is given by

$$\mathbf{F}^{HLLC}_{i+1/2}=\begin{cases}\mathbf{F}_{\mathrm{L}} & \text{if } 0\leqslant S_{\mathrm{L}},\\ \mathbf{F}_{*\mathrm{L}}=\mathbf{F}_{\mathrm{L}}+S_{\mathrm{L}}(\mathbf{Q}_{*\mathrm{L}}-\mathbf{Q}_L) & \text{if } S_{\mathrm{L}}\leqslant 0\leqslant S_*,\\ \mathbf{F}_{*\mathrm{R}}=\mathbf{F}_{\mathrm{R}}+S_{\mathrm{R}}(\mathbf{Q}_{*\mathrm{R}}-\mathbf{Q}_R) & \text{if } S_*\leqslant 0\leqslant S_{\mathrm{R}},\\ \mathbf{F}_{\mathrm{R}} & \text{if } 0\geqslant S_{\mathrm{R}},\end{cases} \tag{41}$$

where

$$\mathbf{Q}_{*K}=\rho_K\left(\frac{S_K-u_K}{S_K-S_*}\right)\begin{bmatrix}1\\ S_*\\ v_K\\ w_K\\ \frac{E_K}{\rho_K}(S_*-u_K)\left[S_*+\frac{p_K}{\rho_K(S_K-u_K)}\right]\end{bmatrix}$$

for $K=\mathrm{L}$ and $K=\mathrm{R}$.

The wave speeds S_{L}, S_* and S_{R} must be estimated. We use the procedure for pressure–velocity estimates of Section 10.5.2 of [17].

We remark that HLLC flux contains all waves in the Riemann problem solution, does not use linearization of the equations and works well for low-density problems and sonic points without any fixes.

4.2. Upwind MUSTA fluxes

In general, the good accuracy of Godunov-type fluxes results from the opening of the Riemann fan and picking up a single value at cell interface $x_{i+1/2}$. Complete (exact or approximate) Riemann solvers recognize all waves in the Riemann fan and therefore provide good resolution of delicate features of the flow, such as contact discontinuities and shear waves. Incomplete Riemann solvers do not recognize the intermediate waves in the Riemann fan and lump them all in one (averaged) state. Centred fluxes can be regarded as very rough Riemann solvers in which the Riemann fan is not opened at all. As a result, the resolution of all intermediate waves and associated flow features by incomplete and centred fluxes is very poor; e.g. contact discontinuities are smeared in time considerably.

A very simple and general approach to the construction of numerical fluxes, which combines the simplicity of centred fluxes and the good accuracy of the Godunov method, is the Multi-Stage (MUSTA) approach [18]. The key idea of MUSTA is to open the Riemann fan by evolving in time the initial data $\mathbf{Q}_{\mathrm{L}}$, $\mathbf{Q}_{\mathrm{R}}$ via the governing equations and a predictor flux and can be explained as follows.

Assume we know the values $\mathbf{Q}_{\mathrm{L}}^{(l)}$, $\mathbf{Q}_{\mathrm{R}}^{(l)}$, adjacent to the interface $x_{i+1/2}$, at the stage l. Integrating (39) over the left $[x_{i+1/2}-\Delta x, x_{i+1/2}]\times[0,\Delta t]$ and right $[x_{i+1/2}, x_{i+1/2}+\Delta x]\times[0,\Delta t]$ control volumes we obtain the following relations:

$$\begin{aligned}
\mathbf{Q}_{\mathrm{L}}^{(l+1)} &= \mathbf{Q}_{\mathrm{L}}^{(l)} - \frac{\Delta t}{\Delta x}\left[\mathbf{F}_{i+1/2}^{(l)} - \mathbf{F}_{\mathrm{L}}^{(l)}\right], \quad \mathbf{F}_{\mathrm{L}}^{(l)} = \mathbf{F}\left(\mathbf{Q}_{\mathrm{L}}^{(l)}\right),\\
\mathbf{Q}_{\mathrm{R}}^{(l+1)} &= \mathbf{Q}_{\mathrm{R}}^{(l)} - \frac{\Delta t}{\Delta x}\left[\mathbf{F}_{\mathrm{R}}^{(l)} - \mathbf{F}_{i+1/2}^{(l)}\right], \quad \mathbf{F}_{\mathrm{R}}^{(l)} = \mathbf{F}\left(\mathbf{Q}_{\mathrm{R}}^{(l)}\right).
\end{aligned} \tag{42}$$

Here we set $\mathbf{F}_{K}^{(l)} = \mathbf{F}(\mathbf{Q}_{K}^{(l)})$, $K=\mathrm{L,R}$, on the grounds that the Riemann-like data extends to $\pm\infty$. The flux $\mathbf{F}_{i+1/2}^{(l)}$ is computed using the evolved data at stage l

$$\mathbf{F}_{i+1/2}^{(l)} = \mathbf{F}^{\mathrm{pred}}\left(\mathbf{Q}_{\mathrm{L}}^{(l)}, \mathbf{Q}_{\mathrm{R}}^{(l)}\right), \tag{43}$$

where $\mathbf{F}^{\mathrm{pred}}$ is the predictor first order flux used in the construction of the MUSTA flux. The time marching procedure is stopped when the desired number of stages k is reached. The final MUSTA flux is

$$\mathbf{F}_{i+1/2}^{\mathrm{MUSTA}} = \mathbf{F}^{\mathrm{pred}}\left(\mathbf{Q}_{\mathrm{L}}^{(k)}, \mathbf{Q}_{\mathrm{R}}^{(k)}\right). \tag{44}$$

In this paper we use the flux of the First-Order Centred (FORCE) Scheme [16,17] as the predictor flux. It can be shown [16,17] that the numerical viscosity of the FORCE flux is smaller than that of the Lax–Friedrichs flux by a factor of two. Recently, the FORCE scheme has been shown to be convergent for some 2×2 nonlinear systems of hyperbolic conservation laws [3].

The procedure to evaluate the MUSTA flux can now be summarized as follows. The multi-stepping is started by setting $\mathbf{Q}_{\mathrm{L}}^{(0)} \equiv \mathbf{Q}_{\mathrm{L}}$, $\mathbf{Q}_{\mathrm{R}}^{(0)} \equiv \mathbf{Q}_{\mathrm{R}}$ for the initial stage $l=0$. Then we do

1. Compute the FORCE flux on data at the stage l

$$\begin{aligned}
\mathbf{Q}^{1/2} &= \frac{1}{2}\left(\mathbf{Q}_{\mathrm{L}}^{(l)} + \mathbf{Q}_{\mathrm{R}}^{(l)}\right) - \frac{1}{2}\frac{\Delta t}{\Delta x}\left(\mathbf{F}\left(\mathbf{Q}_{\mathrm{R}}^{(l)}\right) - \mathbf{F}\left(\mathbf{Q}_{\mathrm{L}}^{(l)}\right)\right),\\
\mathbf{F}_{i+1/2}^{(l)} &= \frac{1}{4}\left(\mathbf{F}(\mathbf{Q}_{\mathrm{L}}^{(l)}) + 2\mathbf{F}(\mathbf{Q}^{1/2}) + \mathbf{F}(\mathbf{Q}_{\mathrm{R}}^{(l)}) - \frac{\Delta x}{\Delta t}\left(\mathbf{Q}_{\mathrm{R}}^{(l)} - \mathbf{Q}_{\mathrm{L}}^{(l)}\right)\right).
\end{aligned} \tag{45}$$

2. If the desired number of time steps k has been reached (that is $l \equiv k$) then the computation of the MUSTA flux is complete and the final flux is given by $\mathbf{F}_{i+1/2} = \mathbf{F}_{i+1/2}^{(k)}$.
3. Otherwise, continue to open the Riemann fan using (42).
4. Goto to step 1.

Practical experience suggests that a number of stages k between 2 and 3 gives numerical results that are comparable with those from the most accurate of fluxes, namely, the first-order Godunov upwind flux used in conjunction with the exact Riemann solver [18]. In this paper we use $k=2$ throughout.

Concerning efficiency, it is found that, for the one-dimensional Euler equations for ideal gases, the cost of such a flux is comparable to that of typical existing approximate Riemann solvers. For real gases it is expected to be more efficient. Moreover, in WENO schemes the reconstruction step accounts for most of the floating point operations so that the difference in the computational cost between schemes with different fluxes becomes negligible.

We remark that the MUSTA scheme stems from the idea of solving numerically the local Riemann problem with a mesh of two cells and applying transmissive boundary conditions at each stage. See [18] for more details.

5. Numerical results

In this section we present numerical results of our schemes as applied to the compressible Euler equations (1) and (40) in one, two and three space dimensions. with the piece-wise parabolic ($r = 3$) and piece-wise cubic ($r = 4$) reconstructions given by (23)–(36). We have also implemented and run the schemes with higher order reconstructions ($r = 5, 6$); the results are omitted. We denote the schemes with the flux X as WENO-X, e.g. the scheme with HLLC flux will be denoted as WENO-HLLC. For comparisons we also run the finite-volume scheme of Shi et al. [14] with dimension-by-dimension piece-wise parabolic ($r = 3$) reconstruction. This scheme uses the upwind Rusanov flux [13] as the building block and a three-point Gaussian quadrature to discretize fluxes and thus is of formal fifth order of accuracy in space.

An important issue is the choice of the Courant number defining the time step. We remark that it seems to have become a popular practice to demonstrate the formal order of *spatial accuracy* of WENO schemes by choosing the time step in such a way that the spatial order dominates the computation. For example, when the third order Runge–Kutta method (8) is used the time step is chosen according to

$$\Delta t \approx \Delta x^{(2r-1)/3}. \tag{46}$$

We have run our schemes with such a time step and obtained good results. However, it should be noted that the use of (46) results in exceedingly small time steps and therefore *enormous* computational cost of the scheme. This is especially so in multiple space dimensions. For example, take $r = 4$, then (46) becomes $\Delta t \approx \Delta x^{7/3}$ which is more stringent than the stability condition for parabolic equations.

For hyperbolic equations the natural choice of the time step is the one resulting from the use of a fixed Courant number. From the point of efficiency it should be as close as possible to the maximum range allowed by the stability condition (10)–(12). In this paper our goal is to assess the performance of our methods, as they would be used in practical computations. We run all convergence tests with a fixed Courant number, which is chosen to be $C_{\mathrm{cfl}} = 0.45$ in two space dimensions and $C_{\mathrm{cfl}} = 0.27$ in three space dimensions.

We evaluate the accuracy and robustness of our methods as applied to four test problems.

5.1. Modified shock/turbulence interaction

This test problem is a variation of the shock/turbulence problem used in [1,7]. We solve the Euler equations (1) and (40) with the following initial condition defined on $[-5, 5]$

$$(\rho, u, p) = \begin{cases} (1.515695, 0.523346, 1.80500), & x < -4.5, \\ (1 + 0.1 \sin 20\pi x, 0.0, 1.), & x > -4.5, \end{cases} \tag{47}$$

which consists of a right facing shock wave of Mach number 1.1 impinging into a high-frequency density perturbation. As the shock moves the perturbation spreads upstream. We compute the flow at the output time $t = 5$, which is more than 10 times larger than that of the standard shock/turbulence problem [1]. The solution contains physical oscillations which have to be resolved by the numerical method.

Fig. 1 shows results of all schemes on a mesh of 2000 cells. A Courant number $C_{\mathrm{cfl}} = 0.6$ is used. In all figures symbols denote the numerical solution and the solid line denotes the reference solution computed on a very fine mesh using the WENO-HLLC scheme. We show only the part of the solution which contains the smooth structures and the moving shock wave. We see that on the given mesh the WENO scheme of Shi et al. [14] severely damps the acoustic disturbance which spreads upstream of the shock. The WENO-HLLC and WENO-MUSTA schemes are more accurate by a factor of two and are superior to the WENO scheme of Shi et al. [14].

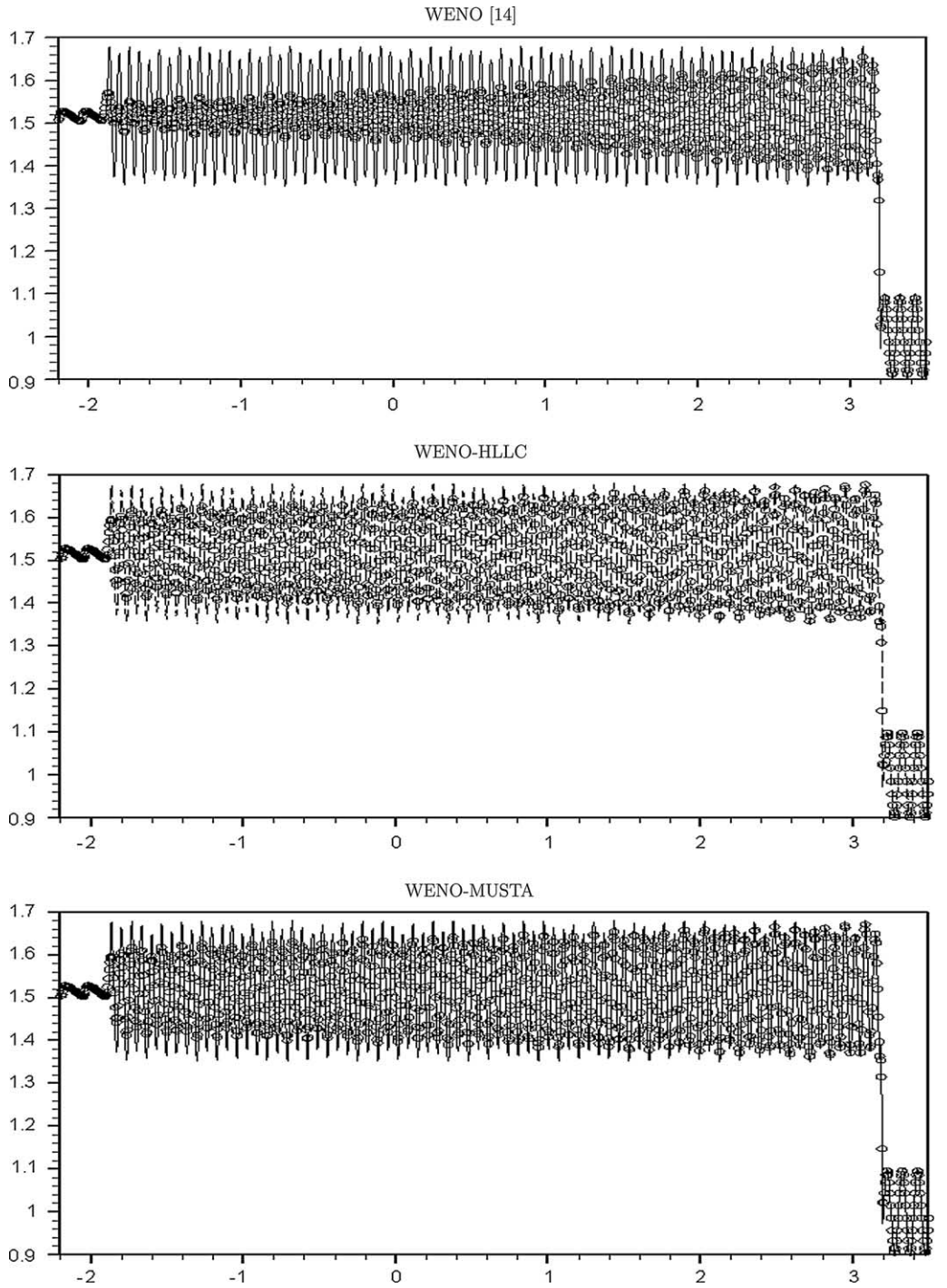

Fig. 1. Computed (symbol) and reference (line) solutions for the Euler equations (1) and (40) with initial condition (47) at output time $t = 5$. Schemes with piece-wise parabolic ($r = 3$) reconstruction. $C_{\mathrm{cfl}} = 0.6$ and $N = 2000$ cells are used for all schemes.

5.2. Two-dimensional vortex evolution problem

We solve the two-dimensional Euler equations with the initial conditions, corresponding to a smooth vortex, moving at 45° to the Cartesian mesh lines. This test problem is from [1] where it is used to study the convergence properties of finite-difference WENO schemes. The problem is solved in the square domain $[-5{:}5] \times [-5{:}5]$ with periodic boundary conditions. The vortex is defined as the following isentropic perturbation to the uniform flow of unit values of primitive variables:

$$\begin{aligned} &u = 1 - \frac{\varepsilon}{2\pi} e^{\frac{1}{2}(1-r^2)} y, \quad v = 1 + \frac{\varepsilon}{2\pi} e^{\frac{1}{2}(1-r^2)} x, \\ &T = 1 - \frac{(\gamma-1)\varepsilon^2}{8\gamma\pi^2} e^{(1-r^2)}, \quad \frac{p}{\rho^\gamma} = 1, \end{aligned} \tag{48}$$

where $r^2 = x^2 + y^2$ and the vortex strength is $\varepsilon = 5$. We compute the numerical solution at the output time $t = 10$ which corresponds to one time period; at this time the vortex returns to the initial position. We use $C_{\mathrm{cfl}} = 0.45$ for all runs.

Table 1 shows the convergence study for schemes with the piece-wise parabolic ($r = 3$) reconstruction. The errors of cell averages of the solution in L_∞ and L_1 norms are presented. We observe that approximately fifth order of accuracy is achieved by all schemes. This order is higher than expected from the use of the third order Runge–Kutta method due to the fact that this problem, *for the given output time*, is more sensitive to spatial accuracy than time discretization. Despite the use of the higher-order (sixth order) Gaussian quadrature for the flux integration, the WENO scheme of Shi et al. [14] is less accurate than the other schemes by a factor of two.

Table 2 shows the convergence study for schemes with the piece-wise cubic ($r = 4$) reconstruction. We see that for a fixed resolution the accuracy improves by a factor of 10. This more than offsets the additional cost of the higher-order reconstruction as compared to the schemes of Table 1.

It is also interesting to note that for the given meshes the order of accuracy actually exceeds the fourth order which is expected to result from the use of the two-point Gaussian rule for spatial integration.

We have also run a three-dimensional vortex problem with the initial conditions, corresponding to the smooth vortex (48), placed in the y–z plane. The results are essentially the same as in the two-dimensional case and are thus omitted.

Table 1
Density convergence study for the vortex evolution problem (48) at the output time $t = 10$

Method	Mesh	L_∞ error	L_∞ order	L_1 error	L_1 order
WENO [14]	25×25	1.04×10^{-1}		6.92×10^{-1}	
	50×50	1.38×10^{-2}	2.91	4.58×10^{-2}	3.92
	100×100	4.60×10^{-4}	4.91	2.33×10^{-3}	4.30
	200×200	1.67×10^{-5}	4.78	9.05×10^{-5}	4.68
WENO-HLLC	25×25	6.61×10^{-2}		3.85×10^{-1}	
	50×50	9.89×10^{-3}	2.74	2.76×10^{-2}	3.80
	100×100	2.68×10^{-4}	5.21	1.24×10^{-3}	4.47
	200×200	1.08×10^{-5}	4.63	5.09×10^{-5}	4.61
WENO-MUSTA	25×25	5.09×10^{-2}		3.53×10^{-1}	
	50×50	8.63×10^{-3}	2.56	2.28×10^{-2}	3.95
	100×100	2.17×10^{-4}	5.32	9.41×10^{-4}	4.60
	200×200	8.10×10^{-6}	4.74	3.84×10^{-5}	4.62

Schemes with piece-wise parabolic ($r = 3$) reconstruction. $C_{\mathrm{cfl}} = 0.45$ is used for all schemes.

Table 2
Density convergence study for the vortex evolution problem (48) at the output time $t = 10$

Method	Mesh	L_∞ error	L_∞ order	L_1 error	L_1 order
WENO-HLLC	25×25	2.08×10^{-2}		1.62×10^{-3}	
	50×50	9.58×10^{-4}	4.44	5.08×10^{-5}	5.00
	100×100	3.41×10^{-5}	4.81	1.56×10^{-6}	5.02
WENO-MUSTA	25×25	2.85×10^{-2}		2.69×10^{-3}	
	50×50	7.74×10^{-4}	5.20	4.30×10^{-5}	5.97
	100×100	2.83×10^{-5}	4.77	1.30×10^{-6}	5.04

Schemes with piece-wise cubic ($r = 4$) reconstruction. $C_{\mathrm{cfl}} = 0.45$ is used for all schemes.

5.3. Double mach reflection of a strong shock

The setup of the problem is as follows [23]. The computational domain is a rectangle 4 units long and 1 unit wide. At the initial time $t = 0$ a right-moving Mach 10 shock is set up so that its front makes an angle of 60° with the x-axis at $x = 1/6$. Ahead of the shock the gas is at rest with $\rho = 1.4$, $p = 1$. The following boundary conditions are prescribed. The inflow boundary condition is applied at the left vertical boundary $x = 0$ and transmissive boundary condition is used at the right vertical boundary $x = 4$. At the bottom boundary $y = 0$ the exact post-shock values of all gas parameters are set for $0 \leqslant x \leqslant 1/6$ whereas for $1/6 < x \leqslant 4$ reflective boundary conditions are used. The exact motion of the Mach 10 shock is prescribed at the top boundary $y = 1$. The output time is $t = 0.2$.

Figs. 2 and 3 show numerical results of our schemes for three meshes: 480×120, 960×240 and 1920×480 cells. Figs. 4 and 5 show a blow up of the region containing the features of main interests for the same meshes. The numerical results of the WENO scheme of Shi et al. [14] can be found in Fig. 3.4 of [14] and are not repeated here.

The detailed discussion of the flow physics can be found in [23]. At the given output time a complicated flow pattern forms containing two Mach shocks, two slip surfaces and a jet. The second Mach shock is weak and almost vanishes at the point where it meets the first slip surface, originating from the first Mach reflection. The second slip surface can be seen near the bottom wall of the domain and is also rather weak. The jet forms near the point where the first slip surface approaches the bottom wall.

Comparing our results with those in the existing literature [4,7,9,14,23] it is seen that both of our schemes produce the flow pattern generally accepted at present as corrected, on all meshes. All discontinuities are well resolved and correctly positioned. Comparing our new schemes, WENO-HLLC and WENO-MUSTA, we see that the main difference occurs in the resolution of the slip surfaces and the associated jet. This is explained by the numerical flux. The HLLC flux accounts for all waves present in the solution of the Riemann problem, slip surfaces in particular. The MUSTA flux also does, but not so accurately as the HLLC flux.

While studying the numerical results of different methods it is important to realize that the slip surfaces are physically unstable features of the flow. From the point of view of solving the problem numerically the converged solution may be obtained only if the full viscous and heat-conductive Navier–Stokes equations are solved. See e.g. [24] for numerical study of two-dimensional Rayleigh–Taylor instability. When we use the Euler equations, the viscosity is in fact the numerical viscosity of the method and depends on the mesh used. As the mesh is refined, no limiting (converged) solution is found. However, for a given particular mesh the numerical solution may exhibit features, typical of physically unstable flows, but with unknown viscosity. Therefore, more pronounced instability of the solution (rolling of the slip surfaces) means smaller numerical diffusion of the WENO-HLLC scheme as compared to the WENO-MUSTA scheme and the WENO scheme of [14].

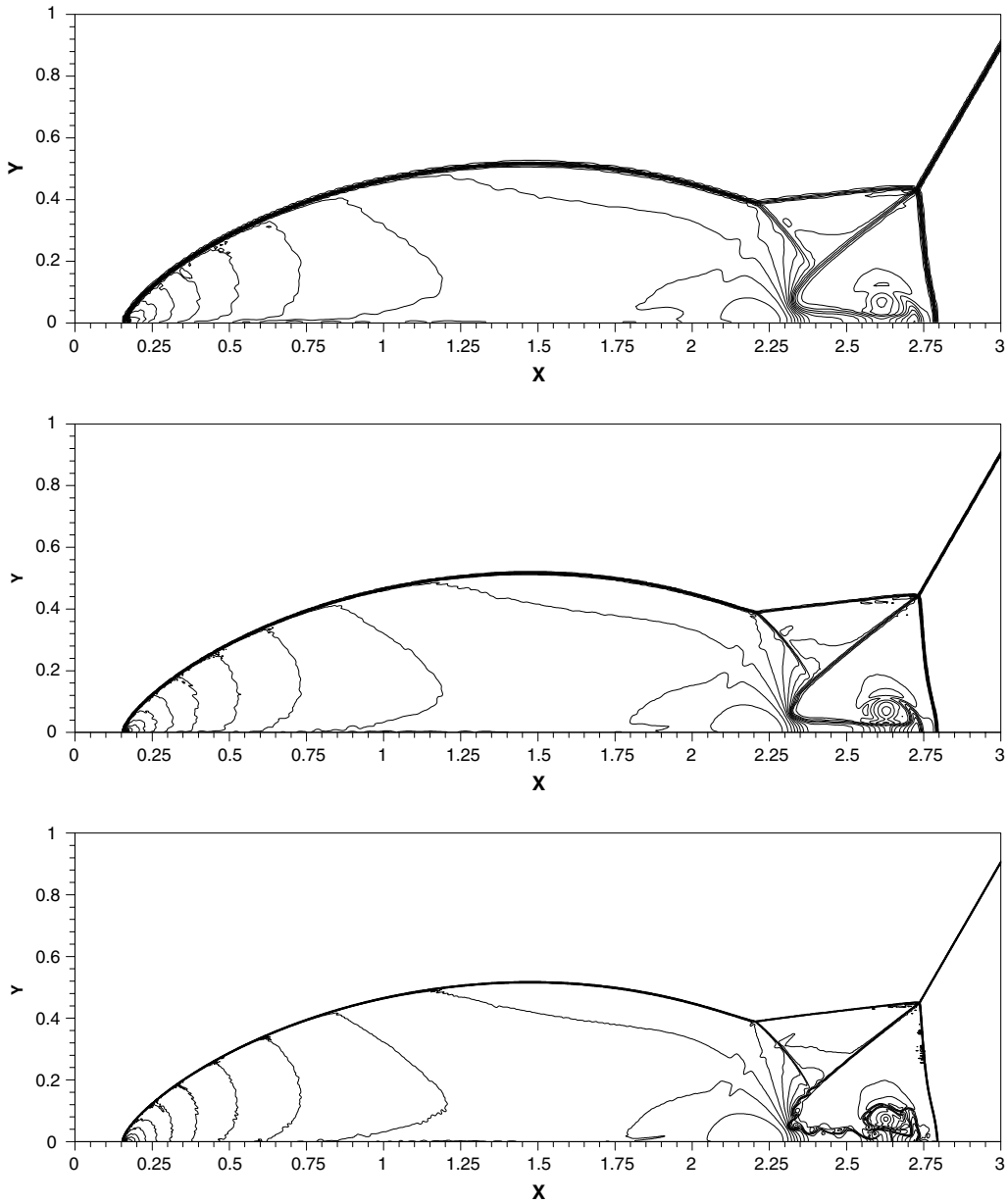

Fig. 2. Density convergence study for the double Mach reflection problem for the WENO-HLLC scheme with the piece-wise parabolic ($r = 3$) reconstruction. Meshes: 480×120, 960×240 and 1920×480 cells. 30 contour lines from 2 to 22.

5.4. Three-dimensional explosion test problem

Finally, we solve the three-dimensional Euler equations of a gamma law gas (1) and (40). The initial condition defined on $[-1{:}1] \times [-1{:}1] \times [-1{:}1]$ consists of two regions of constant but different values of gas parameters separated by a sphere of radius 0.4:

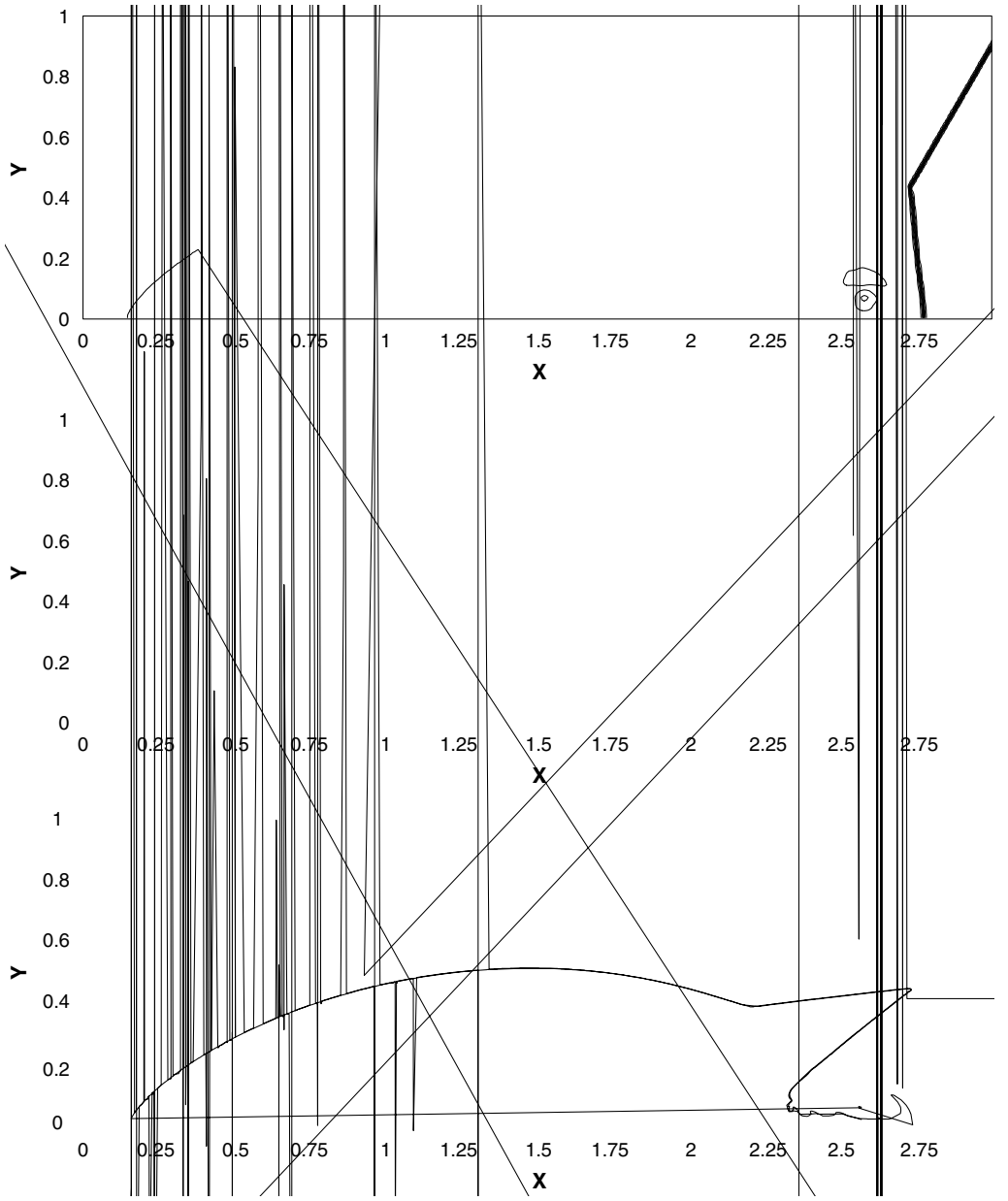

Fig. 3. Density convergence study for the double Mach reflection problem for the WENO-MUSTA scheme with the piece-wise parabolic ($r = 3$) reconstruction. Meshes: Meshes: 480×120, 960×240 and 1920×480 cells. 30 contour lines from 2 to 22.

$$(\rho, p) = \begin{cases} (1.0, 1.0), & r \leqslant 0.4, \\ (0.125, 0.1), & r > 0.4, \end{cases} \quad u = v = w = 0, \quad r^2 = x^2 + y^2 + z^2. \tag{49}$$

This initial condition corresponds to the so-called spherical explosion test problem [17]. We compute the numerical solution at the output time $t = 0.25$ on a mesh of 101 cells in each coordinate direction. We use

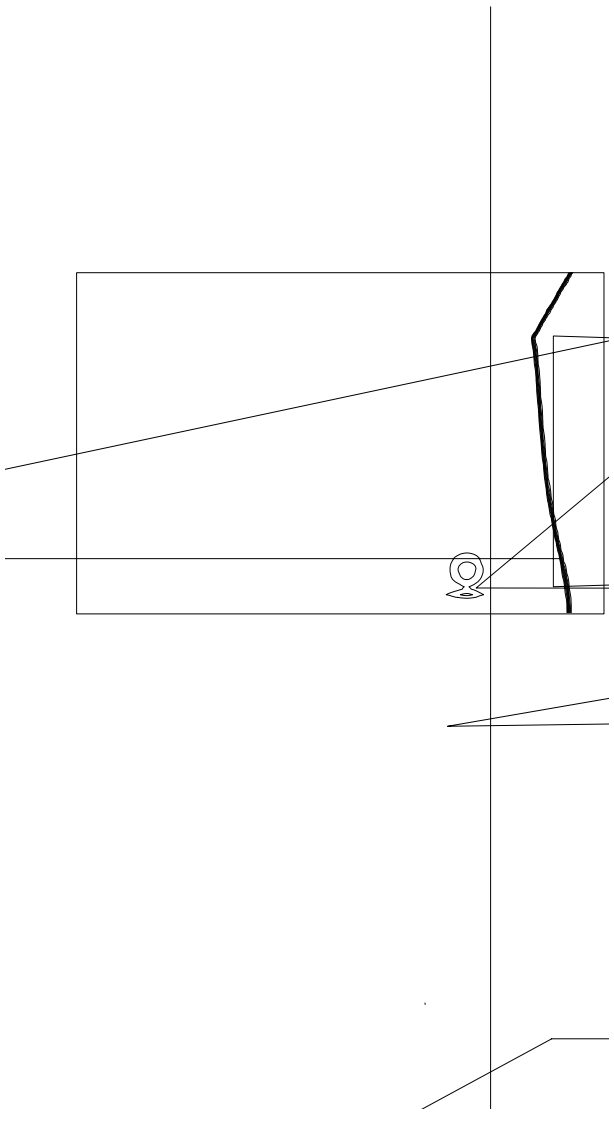

$C_{\text{cfl}} = 0.27$ for all runs. We compare the results of the WENO schemes with a reference radial solution, which is obtained by solving the one-dimensional Euler equations with a geometric source term on a very fine mesh. See Section 17.1 of [17] for details.

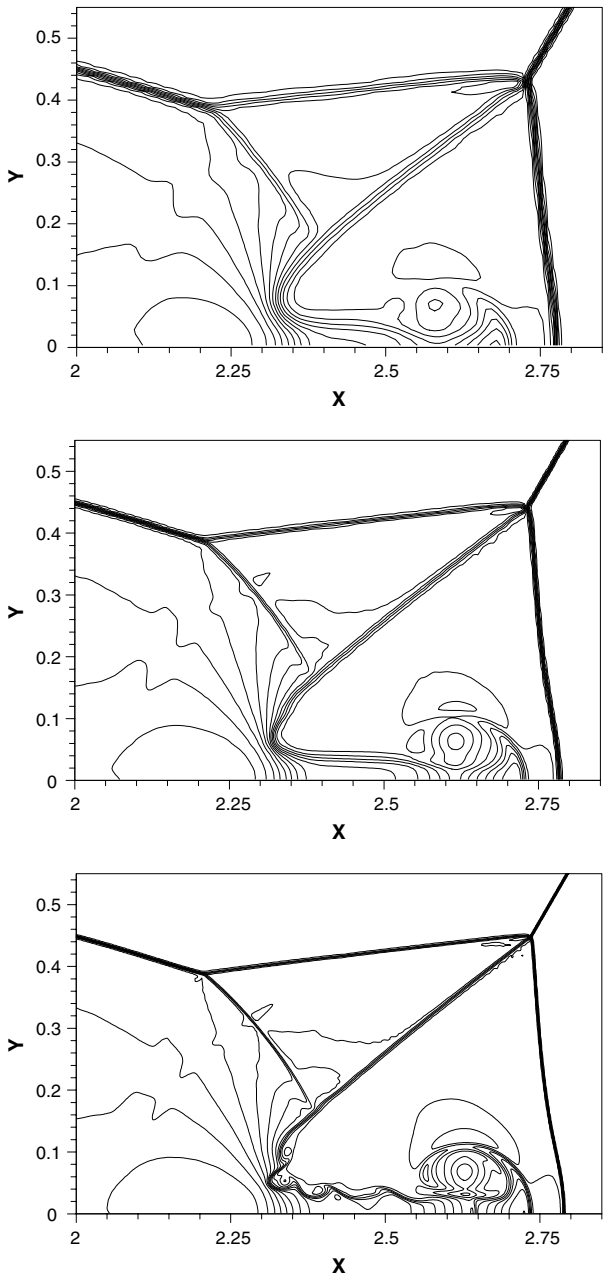

Fig. 5. Density convergence study for the double Mach reflection problem for the WENO-MUSTA scheme with the piece-wise parabolic ($r = 3$) reconstruction. Meshes: 480×120, 960×240 and 1920×480 cells. 30 contour lines from 2 to 22. Zoomed area of Fig. 3.

Figs. 6 and 7 show a comparison between the one-dimensional reference radial solution (solid line) and the cell averages of the three-dimensional WENO solution (symbols) along the radial line that is coincident with the x-axis. We show the results only for $x > 0$. We present distributions of gas density ρ and internal

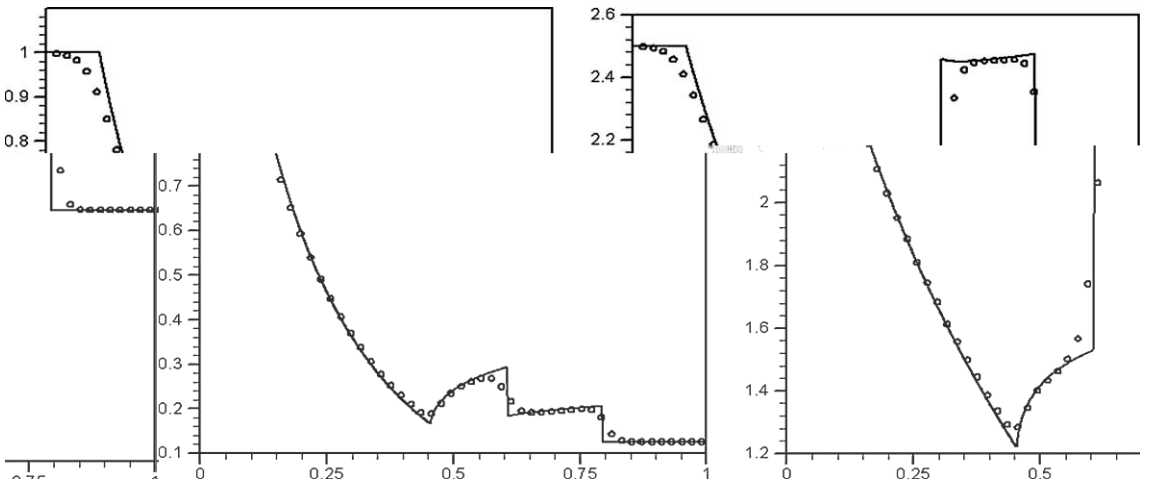

Fig. 6. The spherical explosion test problem. Computed (symbol) and reference (line) solutions of density (left) and internal energy (right) for the WENO-HLLC scheme with piece-wise parabolic reconstruction.

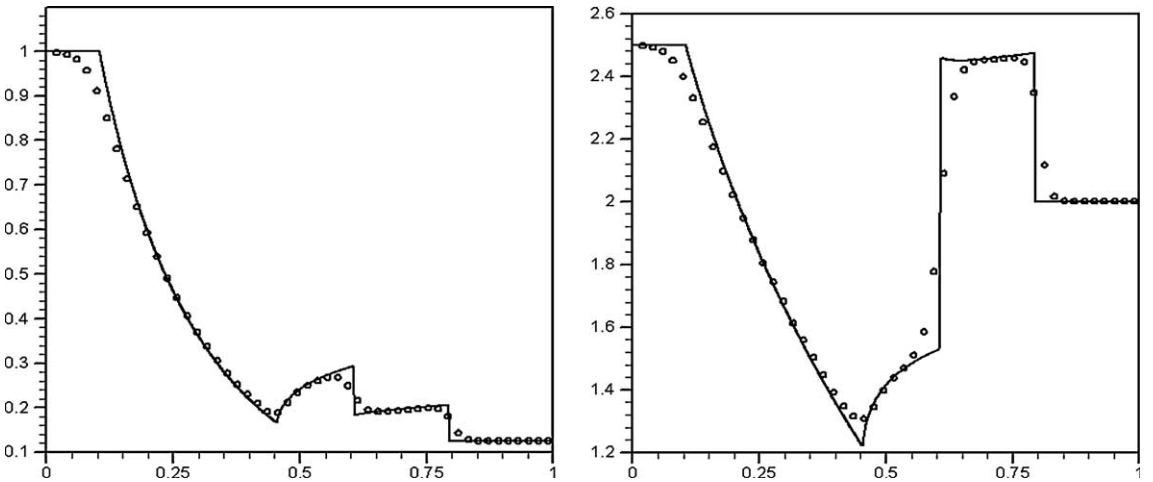

Fig. 7. The spherical explosion test problem. Computed (symbol) and reference (line) solutions of density (left) and internal energy (right) for the WENO-MUSTA scheme with piece-wise parabolic reconstruction.

energy e. The solution contains a spherical shock wave and a contact surface travelling away from the centre and a spherical rarefaction wave travelling towards the origin $(0, 0, 0)$. We observe that all schemes obtain the correct solution with the correct values behind the shock wave and the contact surface.

5.5. Cost comparison of the schemes

Our numerical experiments show that for the piece-wise parabolic reconstruction (fifth order of spatial accuracy) in two space dimensions our finite-volume WENO schemes have essentially the same computational cost as the WENO scheme of Shi et al. [14]. In three space dimensions our schemes are expected to

become faster than the WENO scheme of [14] due to the smaller number of the Gaussian integration points needed for flux integration over the cell face in (5).

A discussion on cost comparison of finite-difference and finite-volume WENO schemes can be found in a number of references, e.g. in [22]. It is stated that when the piece-wise parabolic reconstruction is used in two space dimensions the finite-volume WENO schemes [14] are approximately three times slower than the corresponding finite-difference WENO schemes [7]. In three space dimensions the difference in cost between finite-difference and finite-volume WENO schemes is probably more substantial.

However, despite the higher computational cost, the finite-volume schemes have their advantages. They can be applied on more general unstructured meshes, e.g. on triangular meshes [9,14] whereas finite-difference schemes are restricted to smooth structured meshes. In addition, we remark that the WENO-MUSTA scheme can be applied to hyperbolic systems for which the characteristic information is not known whereas the flux splitting in the finite-difference schemes requires the knowledge of eigenvectors and eigenvalues.

6. Conclusions

In this paper we first carried out an extension of the existing finite-volume WENO schemes to three space dimensions. We provided all necessary information for the reconstruction step of schemes with piece-wise parabolic (fifth order) and piece-wise cubic (seventh order) reconstructions so that they can be easily coded. Then we proposed to use the HLLC and MUSTA fluxes as the building block in the WENO schemes. The upwind HLLC flux is a conventional (one-stage) flux which has successfully been used in the past for the construction of TVD schemes. The MUSTA flux is a very recent multi-stage upwind flux which does not need any information on the details of Riemann problem solution.

We presented the numerical results of the new WENO-HLLC and WENO-MUSTA schemes in one, two and three space dimensions. They suggest that the proposed schemes are more accurate than the existing finite-volume scheme of Shi et al. [14], due to the more accurate fluxes used as the building block.

A particularly useful scheme is the WENO-MUSTA scheme as it combines the simplicity of centred WENO schemes and accuracy of upwind WENO schemes with complete Riemann solvers. The advantages of the WENO-MUSTA scheme will be fully realised when solving very complex hyperbolic systems such as those arising in multi-phase flows, magnetohydrodynamics and general relativity.

Acknowledgements

The authors thank Professor C.-W. Shu for many valuable discussions on WENO reconstruction and the setup of the double Mach reflection problem. Part of the paper was finalized during the stay of the first author at the Isaac Newton Institute for Mathematical Sciences, University of Cambridge and participation in the programme *Nonlinear Hyperbolic Waves in Phase Dynamics and Astrophysics*. The second author acknowledges the support provided by the Isaac Newton Institute for Mathematical Sciences, University of Cambridge, UK, as co-organizer of the six-month programme on *Nonlinear Hyperbolic Waves in Phase Dynamics and Astrophysics*, January to July 2003, and the associated EPSRC senior visiting fellowship, Grant No. GR N09276.

References

[1] D.S. Balsara, C.W. Shu, Monotonicity preserving weighted essentially non-oscillatory schemes with increasingly high order of accuracy, J. Comput. Phys. 160 (2000) 405–452.

[2] J. Casper, H. Atkins, A finite-volume high order ENO scheme for two dimensional hyperbolic systems, J. Comput. Phys. 106 (1993) 62–76.
[3] G.Q. Chen, E.F. Toro, Centred schemes for nonlinear hyperbolic equations, Preprint NI03046-NPA, Isaac Newton Institute for Mathematical Sciences, University of Cambridge, UK, 2003, 31p.
[4] B. Cockburn, C.-W. Shu, Runge–Kutta discontinuous Galerkin methods for convection-dominated problems, J. Sci. Comput. 16 (2001) 173–261.
[5] S.K. Godunov, A finite difference method for the computation of discontinuous solutions of the equation of fluid dynamics, Mat. Sb. 47 (1959) 357–393.
[6] F. Grasso, S. Pirozzoli, Shock wave-thermal inhomogeneity interactions: analysis and numerical simulations of sound generation, Phys. Fluids 12 (1) (2000) 205–219.
[7] G.S. Jiang, C.W. Shu, Efficient implementation of weighted ENO schemes, J. Comput. Phys. 126 (1996) 202–212.
[8] A. Harten, B. Engquist, S. Osher, S.R. Chakravarthy, Uniformly high order accurate essentially non-oscillatory schemes III, J. Comput. Phys. 71 (1987) 231–303.
[9] C. Hu, C.-W. Shu, Weighted essentially non-oscillatory schemes on triangular meshes, J. Comput. Phys. 150 (1999) 97–127.
[10] N.E. Kolgan, Application of the minimum-derivative principle in the construction of finite-difference schemes for numerical analysis of discontinuous solutions in gas dynamics, Uchenye Zapiski TsaGI [Sci. Notes Central Inst. Aerodyn.] 3 (6) (1972) 68–77 (in Russian).
[11] N.E. Kolgan, Finite-difference schemes for computation of three dimensional solutions of gas dynamics and calculation of a flow over a body under an angle of attack, Uchenye Zapiski TsaGI [Sci. Notes Central Inst. Aerodyn.] 6 (2) (1975) 1–6 (in Russian).
[12] X.D. Liu, S. Osher, T. Chan, Weighted essentially non-oscillatory schemes, J. Comput. Phys. 115 (1994) 200–212.
[13] V.V. Rusanov, Calculation of interaction of non-steady shock waves with obstacles, USSR J. Comput. Math. Phys. 1 (1961) 267–279.
[14] J. Shi, C. Hu, C.-W. Shu, A technique for treating negative weights in WENO schemes, J. Comput. Phys. 175 (2002) 108–127.
[15] C.-W. Shu, Total-variation-diminishing time discretizations, SIAM J. Sci. Stat. Comput. 9 (1988) 1073–1084.
[16] E.F. Toro, On Glimm-related schemes for conservation laws, Technical Report MMU-9602, Department of Mathematics and Physics, Manchester Metropolitan University, UK, 1996.
[17] E.F. Toro, Riemann Solvers and Numerical Methods for Fluid Dynamics, second ed., Springer, Berlin, 1999.
[18] E.F. Toro, Multi-stage predictor–corrector fluxes for hyperbolic equations, Preprint NI03037-NPA, Isaac Newton Institute for Mathematical Sciences, University of Cambridge, UK.
[19] E.F. Toro, M. Spruce, W. Speares, Restoration of the Contact Surface in the HLL Riemann Solver, Report CoA 9204, June 1992, Department of Aerospace Science, College of Aeronautics, Cranfield Institute of Technology, England.
[20] E.F. Toro, M. Spruce, W. Speares, Restoration of the Contact Surface in the Harten-Lax–van Leer Riemann solver, J. Shock Waves 4 (1994) 25–34.
[21] B. van Leer, Towards the ultimate conservative difference scheme V: a second order sequel to Godunov' method, J. Comput. Phys. 32 (1979) 101–136.
[22] T. Zhou, Y. Li, C.-W. Shu, Numerical comparison of WENO finite volume and Runge–Kutta discontinuous Galerkin methods, J. Sci. Comput. 16 (2001) 145–171.
[23] P. Woodward, P. Colella, The numerical simulation of two-dimensional fluid flow with strong shocks, J. Comput. Phys. 54 (1984) 115–173.
[24] Y.-T. Zhang, J. Shi, C.-W. Shu, Y. Zhou, Numerical viscosity and resolution of high-order weighted essentially nonoscillatory schemes for compressible flows with high Reynolds numbers, Phys. Rev. E 68 (2003) 1–16, article number 046709.